Research Article Vol. 41, No. 8 / August 2024 / Journal of the Optical Society of America B 1789

Journal of the Optical Society of America B

OPTICAL PHYSICS

Non-transverse electromagnetic fields in micro- and nano-fibers

U. Saglam[1,*] and D. D. Yavuz[1,2]

[1]Department of Physics, University of Wisconsin—Madison, 1150 University Avenue, Madison, Wisconsin 53706, USA
[2]yavuz@wisc.edu
*usaglam@wisc.edu

Received 16 February 2024; revised 31 May 2024; accepted 1 June 2024; posted 25 June 2024; published 18 July 2024

We present an analytical and numerical study of electromagnetic modes in micro- and nano-fibers (MNFs) where the electric and magnetic fields of the modes are not necessarily orthogonal to each other. We first investigate these modes for different fiber structures including circular- and rectangular-core fibers as well as photonic crystal fibers. We then discuss two specific applications of these modes: (1) generation of hypothetical axions that are coupled to the electromagnetic fields through the dot product of electric and magnetic fields of a mode, $\vec{E}\cdot\vec{B}$, and (2) a new type of optical trap (optical tweezers) for chiral atoms with magneto-electric cross coupling, where the confining potential again is proportional to $\vec{E}\cdot\vec{B}$.

https://doi.org/10.1364/JOSAB.521769

1. INTRODUCTION

In recent decades, the developments in fiber-optic communication paved the way for much progress in both the physics and applications of sub-wavelength diameter waveguiding structures [1,2]. The guiding of light in these structures typically requires smooth, adiabatically deformed spatial profiles for the refractive index [1,3]. The evanescent field from these structures can be utilized for shorter response times, better resolutions, and low power consumption sensors [1,4] as well as for trapping, guiding. and reflecting of neutral atoms in the evanescent field of the guided light [5–17]. In addition to trapping, the MNFs can also be utilized for the enhancement and measurement of the quadrupole transitions of atoms, for example, alkali atoms cesium (Cs) and rubidium (Rb) [18–22].

Sub-wavelength waveguiding structures can be fabricated by tapering of hydrogen-flame-heated quartz fiber [1], a method we have also utilized in some of our group's experiments [23,24]. When analyzing the propagation of light in these structures, one needs to design fibers with propagating modes that are beyond the weakly guiding limit where slowly varying approximation fails [2,25]. This leads to modes that are typically referred to as hybrid propagating modes, which are combinations of the more-usual transverse-electric (TE) and transverse-magnetic (TM) modes. These modes' electric and magnetic fields start to demonstrate a counter-intuitive non-transverse behavior and the angle between the electric and the magnetic fields, as well as the angles between the fields and the propagation direction, start to deviate from the well-known value of $\pi/2$. While this counter-intuitive behavior is not widely known, several groups discussed the existence of parallel electric and magnetic fields in propagating waves for different structures, some of which can be counter-propagating circularly polarized waves or waves in which the Poynting vector time averages to zero [26–36]. A wave with $E||B$ condition can be produced with three twisted-mode lasers [37–41], and was used to trap neutral sodium atoms in a magneto-optical trap (MOT) [42]. In addition, such fields are prominent in the investigation of force free fields in plasmas [43].

A key feature of non-transverse modes is that because the angle between the electric and the magnetic fields is different from $\pi/2$, the dot product between these fields, $\vec{E}\cdot\vec{B}$, is non-zero. One fundamental application of the scalar field $\vec{E}\cdot\vec{B}$ is in laboratory search for axions and axion-like particles [44–46]. Since their first prediction about four decades ago, the interest in hypothetical axions has been continually growing [47–50]. Light axions or axion-like particles with a mass in the $10^{-6}\ \text{eV} < m < 10^{-2}\ \text{eV}$ range form a compelling candidate for the dark matter in the universe [51–53]. The existence of axions would also solve one of the longstanding theoretical problems in the standard model of particle physics: the so-called strong CP problem [44–46]. The axions interact with the electromagnetic fields through $\vec{E}\cdot\vec{B}$ and this dot product can be used to generate axions in the lab [44,54–56]. In a recent paper from our group, we numerically explored a possible experimental setup where one can generate and detect axions via long MNF structures, and the rate of axion production highly depends on the $\vec{E}\cdot\vec{B}$ term [57].

This paper is organized as follows: we first summarize the analytical and numerical solutions for the hybrid modes in traditional step-index fibers, and demonstrate the behavior

of the $\vec{E}\cdot\vec{B}$ term within and in the vicinity of the fiber core. Second, we numerically explore the behavior of the $\vec{E}\cdot\vec{B}$ term in different structures such as a rectangular waveguide and a photonic crystal fiber. For these numerical investigations, we use the commercially available finite-difference software COMSOL [58]. Finally, we will discuss two specific applications of such non-transverse fiber modes: (1) generation of hypothetical axions that we mentioned in the previous paragraph, and (2) a new type of optical trap (optical tweezers) for chiral atoms with magneto-electric cross coupling, where the confining potential for the atoms is proportional to $\vec{E}\cdot\vec{B}$ [9,12,59].

2. ANALYTICAL CALCULATIONS OF NON-TRANSVERSE FIELDS IN MICROFIBERS

The propagation of light in waveguides and optical fibers has been studied in depth by a number of authors. When the refractive index difference between the core and the cladding is small, ($n_{\text{core}} - n_{\text{clad}} = \Delta n \sim 0$), then the fiber is in the weakly guiding regime (here, the quantities n_{core} and n_{clad} are the refractive indices of the core and the cladding, respectively). In this regime, one can use the paraxial approximation for the propagating waves and the characteristic equation of the fiber is simplified to [60–62]

$$\frac{J_\nu'(u)}{uJ_\nu(u)} = -\frac{K_\nu'(\omega)}{\omega K_\nu(\omega)}, \tag{1}$$

where $u = a\sqrt{k^2 n_{\text{core}}^2 - \beta^2}$ and $\omega = a\sqrt{\beta^2 - k^2 n_{\text{clad}}^2}$ in a fiber of core diameter a with ν being the mode number. In addition, we note that J and K functions are the Bessel function of the first kind and modified Bessel function of the second kind, respectively. The quantity β is the propagation constant and $k = 2\pi/\lambda$ is the magnitude of the wave-vector for the light. When this equation is solved for β, the solution for the desired mode is acquired. Electromagnetic fields under these approximations behave almost as transverse electromagnetic (TEM) waves, having near-zero longitudinal (z-component) of electric and magnetic fields. However, as one starts decreasing the diameter of the fiber, the weakly guiding approximation breaks down and more of the propagating modes acquire non-transverse behavior [2,25,60,62]. In order to find propagating modes in fibers with small core diameters, one needs to increase the difference of the indices of refraction between the core and the cladding (Δn). In a physical context, the propagation of light in fibers with small radii demonstrate hybrid mode behavior [25], which are the fiber modes that contain electric and magnetic fields that have non-zero longitudinal field components. To find the hybrid modes, one needs to produce a more general characteristic equation from the surface boundary conditions $D_{\text{clad}}^{\perp} - D_{\text{core}}^{\perp} = \sigma_{\text{induced}}$ (perpendicular to the surface) and $E_{\text{clad}}^{\parallel} - E_{\text{core}}^{\parallel} = 0$ (parallel to the surface) [2,25,60,62]. The derived characteristic equation is

$$\left[\frac{J_\nu'(u)}{uJ_\nu(u)} + \frac{K_\nu'(\omega)}{\omega K_\nu(\omega)}\right]\left[\frac{J_\nu'(u)}{uJ_\nu(u)} + \left(\frac{n_{\text{clad}}}{n_{\text{core}}}\right)^2 \frac{K_\nu'(\omega)}{\omega K_\nu(\omega)}\right]$$
$$= \nu\left(\frac{1}{u^2} + \frac{1}{\omega^2}\right)\left[\frac{1}{u^2} + \left(\frac{n_{\text{clad}}}{n_{\text{core}}}\right)^2 \frac{1}{\omega^2}\right]. \tag{2}$$

After this characteristic equation is solved, the electric and magnetic fields for the corresponding mode in the core region of a fiber can be found analytically and they are [25,62]

$$\begin{aligned}
E_r &= -i\beta\frac{a}{u}\left[\frac{1-s}{2}J_{\nu-1}\left(\frac{u}{a}r\right) - \frac{(1+s)}{2}J_{\nu+1}\left(\frac{u}{a}r\right)\right]\cos(\nu\theta+\psi),\\
E_\theta &= i\beta\frac{a}{u}\left[\frac{1-s}{2}J_{\nu-1}\left(\frac{u}{a}r\right) + \frac{(1+s)}{2}J_{\nu+1}\left(\frac{u}{a}r\right)\right]\sin(\nu\theta+\psi),\\
E_z &= J_\nu\left(\frac{u}{a}r\right)\cos(\nu\theta+\psi),\\
B_r &= -i\mu_0\omega_0\epsilon_0 n_{\text{core}}^2\frac{a}{u}\\
&\quad\times\left[\frac{1-s_1}{2}J_{\nu-1}\left(\frac{u}{a}r\right) + \frac{(1+s_1)}{2}J_{\nu+1}\left(\frac{u}{a}r\right)\right]\sin(\nu\theta+\psi),\\
B_\theta &= -i\mu_0\omega_0\epsilon_0 n_{\text{core}}^2\frac{a}{u}\\
&\quad\times\left[\frac{1-s_1}{2}J_{\nu-1}\left(\frac{u}{a}r\right) - \frac{(1+s_1)}{2}J_{\nu+1}\left(\frac{u}{a}r\right)\right]\cos(\nu\theta+\psi),\\
B_z &= -\frac{\beta s}{\omega_0}J_\nu\left(\frac{u}{a}r\right)\sin(\nu\theta+\psi),
\end{aligned} \tag{3}$$

where

$$s = \frac{\nu\left(\frac{1}{u^2}+\frac{1}{\omega^2}\right)}{\left[\frac{J_\nu'(u)}{uJ_\nu(u)} + \frac{K_\nu'(\omega)}{\omega K_\nu(\omega)}\right]}, \qquad s_1 = \frac{\beta^2}{k^2 n_{\text{core}}^2}s, \tag{4}$$

and

$$\omega_0 = \frac{2\pi c}{\lambda}. \tag{5}$$

As an example, we solve the full characteristic equation with $a = 0.5\ \mu\text{m}$ along with $n_{\text{clad}} = 1$ and $n_{\text{core}} = 1.46$ with a wavelength of $\lambda = 633\ \text{nm}$, and calculate that the propagation constant for the lowest order hybrid mode (HE_{11}) is $\beta = 13.860 \times 10^6\ \text{m}^{-1}$. The analytically calculated radial profile for the electric field of this hybrid mode is plotted in Fig. 1.

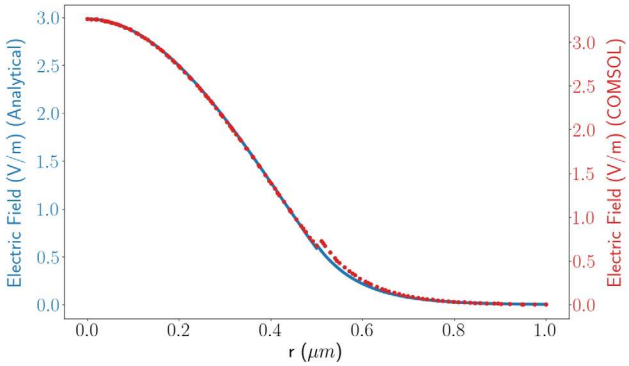

Fig. 1. Plot for the electrical field norm from normalized analytical calculations (solid blue line) and the same electric field data from COMSOL (dotted red line) with $a = 0.5\ \mu\text{m}$, $\nu = 1$, and $\beta = 13.860 \times 10^6\ \text{m}^{-1}$.

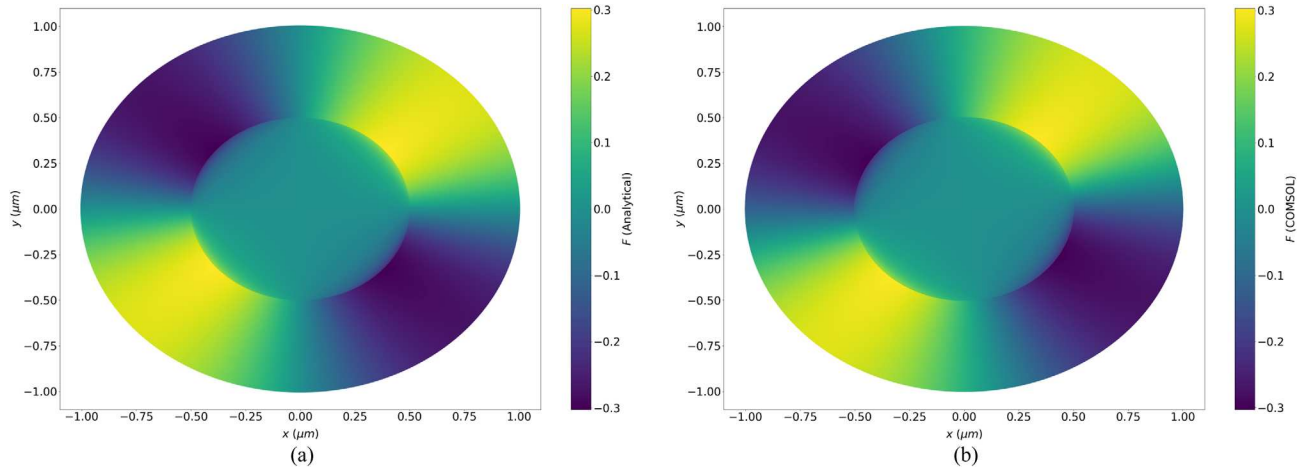

Fig. 2. False-color plot of the scalar field F in the transverse $x-y$ plane within a region of $r=2a$ of the fiber from (a) analytical solutions and (b) COMSOL calculations, with $a=0.5$ μm, $\nu=1$, and $\beta=13.860\times10^6$ m^{-1}. There is good agreement between the two results, both of which show non-smooth behavior at the core-cladding boundary.

While it is possible to analytically calculate these modes for simple step-index structures, this is not the case for more complicated waveguides including photonic crystal fibers. For much of what we discuss below, we will instead rely on numerically calculating these modes using commercial optical-wave simulation software, COMSOL. For comparison, in Fig. 1, we also plot the profile of the electric field for the simple cylindrical step-index structure using COMSOL. As expected, there is very good agreement between the analytical solution and the numerical calculation. The small difference between the results is coming from the data sampling resolution of COMSOL. When a higher resolution mesh is used to sample data, better agreements between the results can be demonstrated. We note that the discontinuity on the E-field occurs from the Maxwell boundary condition $\epsilon\vec{E}_r(a)=\epsilon_0\vec{E}_r(a)$.

In this paper, for various fiber structures that we discuss below, we will focus our attention to the lowest order mode (i.e., the hybrid fundamental mode, HE_{11}), which is described thoroughly in Ref. [2]. For structures that can maintain higher modes, the ratio of power carried by the evanescent field at the cladding and the field at the core can be modified to be higher or lower depending on the application [2,25,62].

Throughout this paper, we will summarize the non-transverse behavior of these waves propagating in the MNFs by examining the scalar field of

$$\begin{aligned}F&\equiv\cos\theta\\&=\frac{\vec{E}\cdot\vec{B}}{|\vec{E}||\vec{B}|}\\&=\frac{E_xB_x^*+E_yB_y^*+E_zB_z^*+E_x^*B_x+E_y^*B_y+E_z^*B_z}{|\vec{E}||\vec{B}|}.\end{aligned}\tag{6}$$

Here, we define the quantity θ, which is the geometric angle between the electric and magnetic field vectors. For simple step-index fiber structures, we can use the solution given in Eq. (3) to analytically calculate this quantity:

$$F=-\frac{\beta\epsilon_0cs\lambda}{4\pi|\vec{E}||\vec{B}|}\left(J_\nu\left(\frac{u}{a}r\right)^2+J_{\nu-1}\left(\frac{u}{a}r\right)J_{\nu+1}\left(\frac{u}{a}r\right)\right)\mathrm{Sin}(2(\nu\theta+\psi)),\tag{7}$$

where the norms of the fields, $|\vec{E}|$ and $|\vec{B}|$, can be written as

$$|\vec{E}||\vec{B}|=\sqrt{|\vec{E}_r|^2+|\vec{E}_\theta|^2+|\vec{E}_z|^2}\sqrt{|\vec{B}_r|^2+|\vec{B}_\theta|^2+|\vec{B}_z|^2}.\tag{8}$$

We plot this scalar field from both analytical calculations [Fig. 2(a)] and from COMSOL [Fig. 2(b)] for the previous microfiber structure that we discussed in Fig. 1. These figures are false-color plots for F in the transverse $x-y$ plane. As seen in these figures, there is again very good agreement between the analytical solution and the numerical calculation from COMSOL, both of which show nonzero values for the F field. The electromagnetic fields start demonstrating non-transverse characteristics close to the core and cladding boundary. In Fig. 3, we plot the radial profile for the scalar field F at a specific azimuthal angle, $F(r,\theta)$ with $\theta=\pi/4$, for both COMSOL (dashed, red) and analytical (solid, blue) results. The results

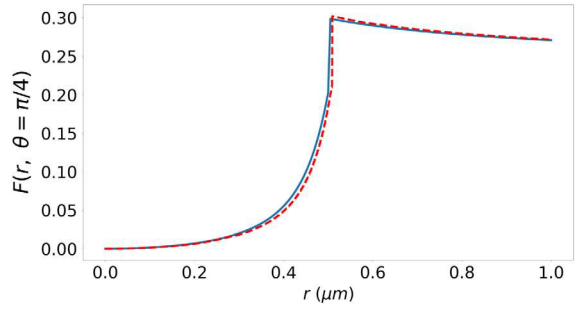

Fig. 3. Plot for $F(r,\theta=\pi/4)$ with $a=0.5$ μm, $\nu=1$ and $\beta=13.860\times10^6$ m^{-1}. The solid blue line is the analytical calculation and the dashed red line is the numerical results from COMSOL. The non-smooth behavior at the core-cladding boundary is due to the imposed Maxwell boundary conditions, where the perpendicular component of the displacement vector is continuous; but not the electric field vector.

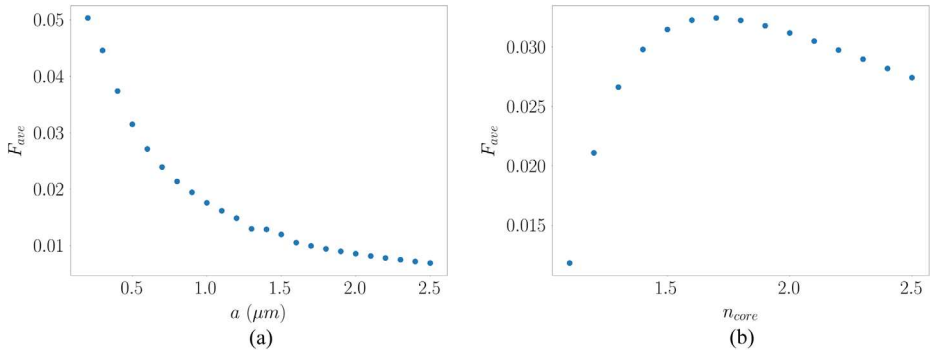

Fig. 4. (a) The plot of the average scalar field, F_{ave}, as a function of fiber core diameter a, for $\nu = 1$ modes with $n_{\text{clad}} = 1$ and $n_{\text{core}} = 1.46$. The scalar field decreases as the core size increases, since waves approach transverse waves propagating in the bulk. (b) The plot of the average scalar field F_{ave} as a function of the core refractive index, n_{core}, for $\nu = 1$ modes with $r_{\text{core}} = 0.5$ μm (the refractive index of the cladding is fixed at $n_{\text{cladding}} = 1$).

match well, both of which show non-smooth behavior at the core-cladding boundary. The non-smooth behavior is due to the imposed Maxwell boundary conditions, where the perpendicular component of the displacement vector is continuous, but not the electric field vector. We observe that the discontinuity in the perpendicular component of the electric field becomes more drastic, as the refractive index difference between the core and the cladding gets larger [62].

A useful quantity that summarizes the non-transverse behavior of a fiber mode is the spatial average of the scalar field, which we define as $F_{\text{ave}} \equiv \int \mathrm{d}x\mathrm{d}y|F(x, y)|/\int \mathrm{d}x\mathrm{d}y$. We expect this spatial average F_{ave} to decrease as the core radius ($r_{\text{core}} = a$) increases, since waves propagating in fibers with a larger core would approach transverse waves propagating in the bulk. To demonstrate this behavior, we increase a and calculate the propagating modes in COMSOL. In Fig. 4(a), we plot this quantity as a function of the core radius a, for the wavelength of light of $\lambda = 1.55$ μm. We have verified that the critical parameter for this type of non-transverse behavior is the ratio λ/a [i.e., the behavior at different wavelengths can be found by using an appropriate scaling of Fig. 4(a)]. We find that, as expected, as the size of the core increases, the largely transverse waves near the central regions of the core result in an overall low value of the averaged scalar field F. We also numerically find that while one can find different modes with different ν and β values, the maximum value of the scalar field F does not vary much between different modes [i.e., the behavior that is plotted in Fig. 4(a) is valid not only for the lowest order mode, but for other modes as well].

We have also numerically investigated the behavior of the scalar field F with respect to the change in the refractive index of the cladding. In Fig. 4(b), we plot the average scalar field, F_{ave}, as a function of n_{clad}, while keeping $r_{\text{core}} = a$ and $n_{\text{core}} = 1.46$ constant. We observe that as n_{core} increases, the spatially averaged field initially gets large, peaks around $n_{\text{core}} = 1.7$, and then shows a slight decrease with further increase of the core refractive index.

3. DIFFERENT STRUCTURES FOR NON-TRANSVERSE EM WAVE SCHEME

In the previous section, we discussed non-transverse electromagnetic waves in a simple step-index fiber geometry where analytical solutions exist and we could, therefore, make comparisons with the numerical solutions using COMSOL. In this section, we will discuss an extension of these results to different waveguide structures including rectangular and photonic-crystal (i.e., structured) fibers.

A. Rectangular Waveguide

Non-transverse EM waves in rectangular and elliptical waveguides may be useful in physical systems where an asymmetrical behavior between the two transverse axes is desired. In our numerical investigations of these systems, we have largely found the results that we have discussed in the previous section to be valid, i.e., we have observed similar behavior for these non-transverse waves as the size of the structure, or the refractive index difference between core and the cladding, is varied. Because of this, we will not present a systematic study of these asymmetric structures. Rather, in this section, we will discuss the results for an asymmetric waveguide, as representative examples of what kind of non-transverse behavior can be expected.

In Fig. 5, we show results for a rectangular waveguide with a core length of 0.75 μm and a core height of 0.5 μm. Here, similar to the previous section we take the core and the cladding refractive indices to be $n_{\text{core}} = 1.46$ and $n_{\text{cladding}} = 1$, and we plot the scalar field F for three different modes. These modes have propagation constants of β's of $= 9.80117 \times 10^6\ \text{m}^{-1}$ [Fig. 5(a)], $9.80862 \times 10^6\ \text{m}^{-1}$ [Fig. 5(b)], and $10.0035 \times 10^6\ \text{m}^{-1}$ [Fig. 5(c)]. In all of these figures, one can see the interesting spatial behavior of the field F, in addition to numerical values as high as 0.4. We have also numerically investigated a fiber with an elliptical core and have found the behavior to be very similar to the circular-core fiber structure that we have discussed above.

B. Photonic Crystal Fibers

Photonic crystal fibers are optical micro- and nano-structures where the index of refraction changes periodically [63,64].

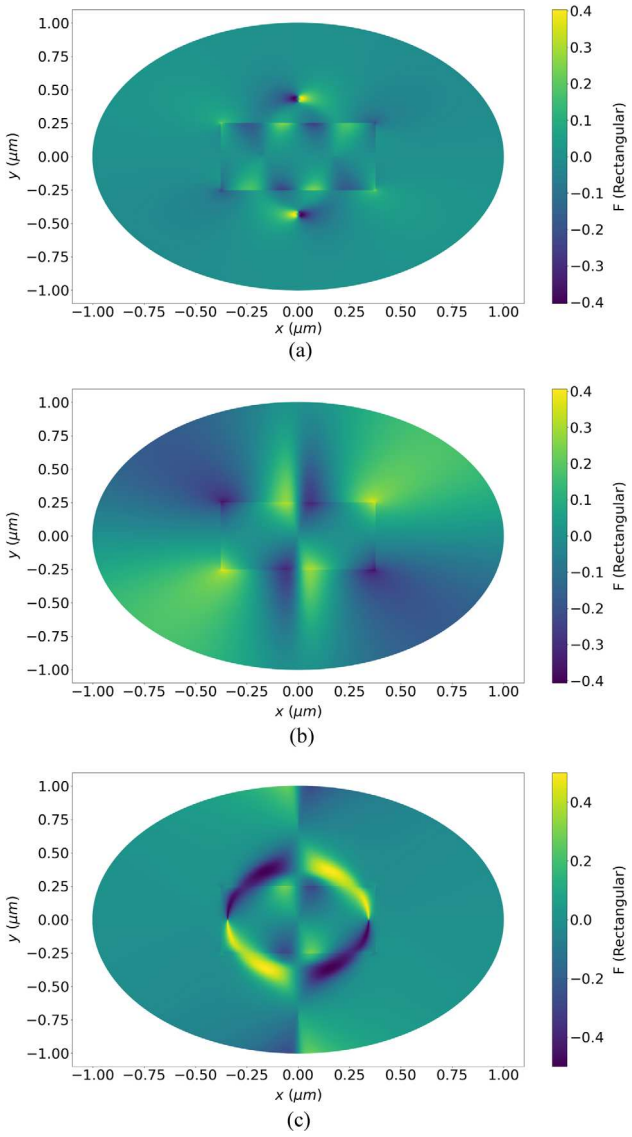

Fig. 5. False-color plot of F (calculated by COMSOL) given by Eq. (6) in a rectangular waveguide structure with $n_{\text{core}} = 1.46$, $n_{\text{clad}} = 1$, length $= 0.75\ \mu\text{m}$, height $= 0.5\ \mu\text{m}$, $\nu = 1$, and β's of (a) $= 10.0035 \times 10^6\ \text{m}^{-1}$, (b) $11.7594 \times 10^6\ \text{m}^{-1}$, and (c) $9.80117 \times 10^6\ \text{m}^{-1}$.

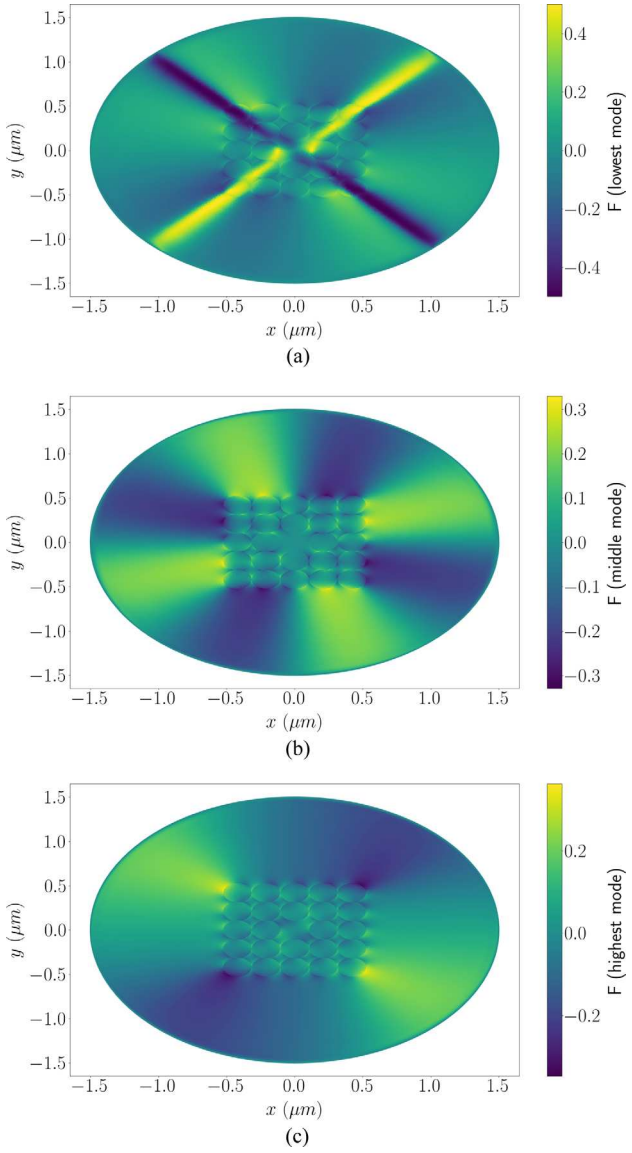

Fig. 6. False-color plot of the scalar field F calculated using Eq. (6) in a 5×5 photonic crystal structure with $n_{\text{core}} = 1.46$, $n_{\text{clad}} = 1$, $a = 0.1\ \mu\text{m}$, $\nu = 1$, and β's of (a) $= 10.5891 \times 10^6\ \text{m}^{-1}$, (b) $11.7207 \times 10^6\ \text{m}^{-1}$, and (c) $12.3381 \times 10^6\ \text{m}^{-1}$. (a) F of the lowest mode of a photonic crystal structure with $a = 0.1\ \mu\text{m}$ from the COMSOL data with β. (b) F of a middle mode of a photonic crystal structure with $a = 0.1\ \mu\text{m}$ from the COMSOL data with β. (c) F of the highest mode of a photonic crystal structure with $a = 0.1\ \mu\text{m}$ from the COMSOL data with β.

Over the last two decades, the interest in these types of fibers has been continually growing, since their performance can substantially exceed traditional fibers. For example, one can manufacture photonic crystal fibers that can be single mode over a large wavelength range, or show highly enhanced optical nonlinearities.

In this section, we will discuss our COMSOL simulations that investigate the behavior of F in an example photonic crystal structure. We consider a photonic crystal fiber with an array of 5×5 cylinders. The diameter of each cylinder is $a = 0.1\ \mu\text{m}$ and the spacing between neighboring cylinders is $0.01\ \mu\text{m}$. The cylinder at the center is missing since we aim to confine the modes near the center of the structure. For a photonic crystal structure seen in Fig. 6, for β's of $= 13.39381 \times 10^6\text{m}^{-1}$ [Fig. 6(a)], $13.39411 \times 10^6\ \text{m}^{-1}$ [Fig. 6(b)], $13.39471 \times 10^6\ \text{m}^{-1}$ [Fig. 6(c)] modes, the scalar field F has a maximum of about 0.3, also with reasonably high values for the F-field near the center of the structure.

We have also investigated the behavior of the average field F_{ave}, as we vary the radius of the core of the cylinders. In Fig. 7(a) we plot the quantity F_{ave}, which is the field F averaged over the area of a circle defined with a radius of $r_{\text{av}} = 5.1 \times \sqrt{2}a$. This circle size is chosen this way to capture all of the 5×5 photonic crystal fiber structure near the center of the fiber, as well as a significant portion of the cladding. The results are not sensitive to the specific choice of the radius of the circle, as long as it is large enough to capture the most of the mode structure. Here,

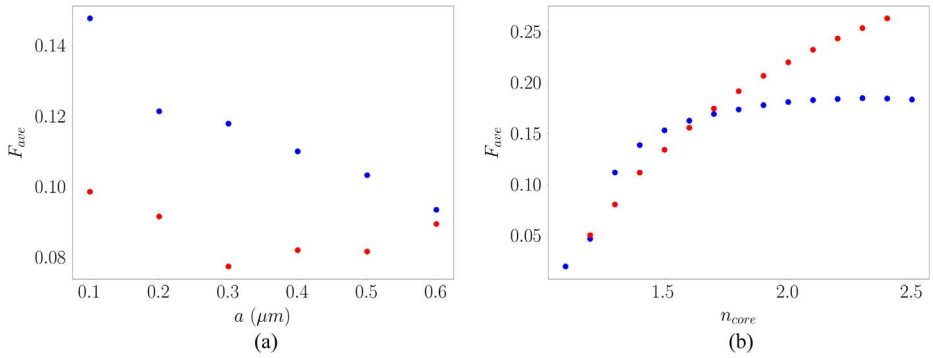

Fig. 7. (a) The plot of F_{ave} averaged over a circular area of $R = 5.1 \times \sqrt{2}a$ versus a single fiber's a for the 5×5 photonic crystal fiber structure. The blue dots are the results for the lowest mode while the red dots are the results for a representative middle mode between the highest and lowest order modes. (b) The plot of F_{ave} averaged over a circular area of $R = 5.1 \times \sqrt{2}a$ versus the index of refraction of the cores n_{core} for the 5×5 photonic crystal fiber structure. The blue dots are the results for the lowest mode while the red dots are the results for a representative middle mode between the highest and lowest order modes.

we plot the results for the lowest mode (blue dots) and as well as a representative middle-level mode (red dots), as we vary the core-radius of the cylinders, a. Here, we observe that the lowest mode has a higher average value of F. We also note that compared to Fig. 4(a), the magnitude of F_{ave} is three times larger for the lowest order modes, while the observed decay behavior is similar. We find that, while performing these calculations in COMSOL, as the cylinder radius a gets larger, the simulation space gets large and rapidly increases the memory requirement of the computation. As an example, for a photonic crystal structure with a single cylinder radius $a = 0.5$ with a coarse mesh, most of the physical 32 GB RAM and around 80 GB of virtual RAM were used and the calculation took around 8–10 h. Since we were working with distances that are comparable to the wavelength of the light, EW frequency domain (EWFD) analysis was required in COMSOL, which takes more time than the beam envelopes (EWBE) analysis [58].

To see the behavior of F_{ave} with respect to n_{core}, we calculate the behavior of F_{ave} in Fig. 7(b) with core radius $a = 0.1$ μm, with blue dots being the lowest order mode and the red dots being a middle mode. Again, here, F_{ave} is larger than a single-cored structure seen in Fig. 4(b), while the overall behavior of the dependence to n_{core} is similar.

4. GENERATION AND DETECTION OF HYPOTHETICAL AXION PARTICLES

Since their first prediction about four decades ago, the interest in hypothetical axions has been continually growing [47–50]. Light axions or axion-like particles with a mass in the 10^{-6} eV $< m <$ 10^{-2} eV range form a compelling candidate for the dark matter in the universe [51–53]. The existence of axions would also solve one of the longstanding theoretical problems in the standard model of particle physics: the so-called strong CP problem [44–46]. Not surprisingly, there has been a large number of experimental efforts to detect this elusive particle. The theoretical proposals exploring axion-photon coupling date back to 1980s [65–67], spurring much experimental work. One set of experiments aims to detect axions that are naturally present in the environment [68–71]. Another set of experiments works towards generating and detecting axions in the lab, and has greater control of the experimental parameters since they do not rely on an external source of axions [72,73]. This set of experiments is cordially referred to as *light shining through a wall (LSW)*, and its sensitivity has been steadily increasing over the last few decades. These experiments rely on generating axions at one side of an optical barrier (i.e., a wall) using lasers, while aiming to detect them at the other side of the barrier.

As we will discuss below in detail, were they to exist, the axions are coupled to the fields of electromagnetics through the $\vec{E} \cdot \vec{B}$ term. In LSW experiments, the generation of axions is typically accomplished by utilizing the interaction of the electric-field of a laser beam with an intense DC magnetic field. As we have noted in a recent publication, such generation could also be accomplished using both the electric field and magnetic field of a laser [57]. This requires a non-vanishing $\vec{E} \cdot \vec{B}$ term due to a laser beam, which requires non-transverse electromagnetic modes. One application of the modes that we have discussed above is, therefore, to the generation of such hypothetical axions.

More specifically, the Klein-Gordon equation for the axion field $\Phi(\vec{r}, t)$ has a driving term that involves the dot product of the electric and magnetic fields:

$$\nabla^2\Phi - \frac{1}{c^2}\frac{\partial^2\Phi}{\partial t^2} - \left(\frac{mc}{\hbar}\right)^2\Phi = \frac{g_{a\gamma\gamma}}{\mu_0 c}\vec{E}\cdot\vec{B}. \tag{9}$$

Here, m is the mass of the hypothetical axion and ∇^2 is the Laplacian operator. The quantity $g_{a\gamma\gamma}$ is the axion-EM coupling constant. As we discussed in our recent paper, the driving $\vec{E} \cdot \vec{B}$ [57] term can be used to confine the generated axion wave, Φ. Using procedures quite similar to finding the optical modes of a fiber [60], the Klein-Gordon equation for the axion field can be reduced to a single radial differential equation, driven by the spatial mode profile of $\vec{E} \cdot \vec{B}$. This radial differential equation can then be numerically integrated to find the shapes of the confined axion modes.

In our recent paper, we assumed the simplest case of only radial dependence of the driving term and therefore found the cylindrically symmetric solutions for the confined axions. For the driving laser beam in a hybrid mode, as shown in Eq. (3),

there is a dependence of the electric and magnetic fields, and therefore $\vec{E}\cdot\vec{B}$ term, on the azimuthal angle θ.

From Eq. (7), since we know the general form of the driving term, we define our trial solution $\Phi(r,\theta,z)$ to be of the form

$$\Phi(r,\theta,z)=u_\phi(r,\theta). \tag{10}$$

Differing from our recent paper where we considered excitation using two different laser beams [57], this solution does not include a propagation term that is dependent on z. This is because both the electric and magnetic fields have the same z-dependent propagation term, which cancels out in the dot product. Consequently, the Klein-Gordon equation of Eq. (9) can be reduced to the following differential equation for $u_\phi(r,\theta)$:

$$\frac{d^2u_\phi}{dr^2}+\frac{1}{r}\frac{du_\phi}{dr}-\frac{1}{r^2}\frac{d^2u_\phi}{d\theta^2}+\left(\frac{mc}{\hbar}\right)^2u_\phi=\frac{g_{a\gamma\gamma}}{\mu_0 c}E(r,\theta)B^*(r,\theta). \tag{11}$$

Next, we define the quantity $\Delta k^2\equiv(mc/\hbar)^2$. With this definition and using the analytical result from Eq. (7) for $E\cdot B$, we obtain

$$\begin{aligned}&\frac{d^2u_\phi}{dr^2}+\frac{1}{r}\frac{du_\phi}{dr}+\frac{1}{r^2}\frac{d^2u_\phi}{d\theta^2}+\Delta k^2u_\phi\\&=\frac{\beta\epsilon_0 s\lambda g_{a\gamma\gamma}}{4\pi}\left(J_\nu\left(\frac{u}{a}r\right)^2+J_{\nu-1}\left(\frac{u}{a}r\right)J_{\nu+1}\left(\frac{u}{a}r\right)\right)\\&\quad\times\mathrm{Sin}(2(\nu\theta+\psi)).\end{aligned} \tag{12}$$

Using separation of variables, we can write our trial solution as $u_\phi(r,\theta)=R_\phi(r)\Theta(\theta)$, where we have defined the function $\Theta(\theta)=\mathrm{Sin}(2(\nu\theta+\psi))$. With this simplification, we obtain the following ordinary differential equation for $R_\phi(r)$ in the core of the fiber:

$$\begin{aligned}&\frac{d^2R_\phi}{dr^2}+\frac{1}{r}\frac{dR_\phi}{dr}-\frac{4\nu^2}{r^2}R_\phi+\Delta k^2R_\phi\\&=\gamma\left(J_\nu\left(\frac{u}{a}r\right)^2+J_{\nu-1}\left(\frac{u}{a}r\right)J_{\nu+1}\left(\frac{u}{a}r\right)\right).\end{aligned} \tag{13}$$

Using a similar procedure, the differential equation for the cladding part of the solution can be written as

$$\begin{aligned}&\frac{d^2R_\phi}{dr^2}+\frac{1}{r}\frac{dR_\phi}{dr}-\frac{4\nu^2}{r^2}R_\phi+\Delta k^2R_\phi\\&=\gamma\left(\frac{J_\nu(u)}{K_\nu(w)}\right)^2\left(K_\nu\left(\frac{w}{a}r\right)^2+K_{\nu-1}\left(\frac{w}{a}r\right)K_{\nu+1}\left(\frac{w}{a}r\right)\right).\end{aligned} \tag{14}$$

Here, we collect all the constants in the axion driving term into a single term and define

$$\frac{\beta\epsilon_0 s\lambda g_{a\gamma\gamma}}{4\pi}=\gamma. \tag{15}$$

We numerically solve Eqs. (13) and (14) using a fourth order Runge-Kutta algorithm for the non-transverse hybrid mode HE_{11} that we have discussed above. We will present two examples for the confined axion mode profiles that are driven by the non-transverse electromagnetic modes. We first use a hybrid HE_{11} mode with $\beta=13.60\times10^6\ \mathrm{m}^{-1}$ of a laser at a wavelength $\lambda=633$ nm in an air clad silica fiber, with the index of refraction of $n_{\mathrm{core}}=1.46$ and a core radius of $a=0.5$ μm. For the axion mass $m=10^{-2}$ eV, the value of Δk^2 is $\Delta k^2=-65.05\times10^6\ \mathrm{m}^{-2}$. The solution of the axion differential equation with these constants can be seen in Fig. 8(a). The difference in the solutions as we scan the axion mass range from $m=10^{-2}$ to $m=10^{-6}$ eVs is around $\gamma\times10^{-8}$, which stays minimal, suggesting some solutions that are not very sensitive to the hypothetical axion mass.

One can engineer the parameters of the fiber and the laser to obtain different spatial structures for the confined axion modes. Another example is shown in Fig. 8(b). In this plot, the fiber structure has a radius of $a=0.3$ μm, and an index of refraction of $n=1.46$, for a laser wavelength of $\lambda=1550$ nm. The mode we choose for this case is the fundamental HE_{11} mode with a propagation constant of $\beta=4.16\times10^6\mathrm{m}^{-1}$. Again, for these parameters we have $\Delta k^2=-65.05\times10^6\ \mathrm{m}^{-2}$.

To demonstrate the 2D behavior of the total field $u_\phi(r,\theta)=R_\phi(r)\Theta(\theta)$, we plot a 2D false color plot of the field $u_\phi(r,\theta)$ in Fig. 9 for the parameters from Fig. 8(b).

The axion wave that is generated through non-transverse electromagnetic modes of a fiber can be detected at another location. One specific strategy is outlined in Ref. [57]. Here, the key idea is that the generated axion wave can leak to a nearby fiber, and can then be detected by interacting with a mixing

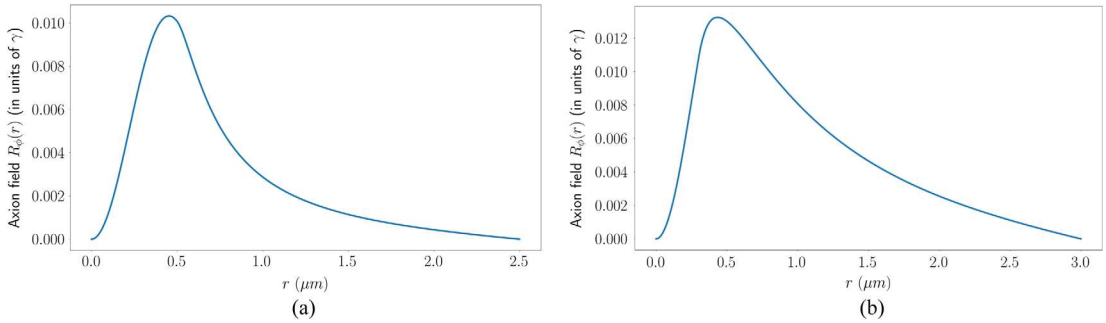

Fig. 8. (a) The solution $R_\phi(r)$ with $\theta=\pi/4$ for the hypothetical axion field for the HE_{11} mode with a propagation constant $\beta=13.60\times10^6\ \mathrm{m}^{-1}$ for an air-clad fiber with radius $a=0.5$ μm and a core index of refraction $n=1.46$ with a laser with wavelength $\lambda=633$ nm and $\Delta k^2=-65.05\times10^6\ \mathrm{m}^{-2}$. (b) The solution $R_\phi(r)$ with $\theta=\pi/4$ for the hypothetical axion field for the HE_{11} mode with a propagation constant $\beta=4.16\times10^6\ \mathrm{m}^{-1}$ for an air-clad fiber with radius $a=0.3$ μm and a core index of refraction $n=1.46$ with a laser with wavelength $\lambda=1550$ nm and $\Delta k^2=-65.05\times10^6\ \mathrm{m}^{-2}$.

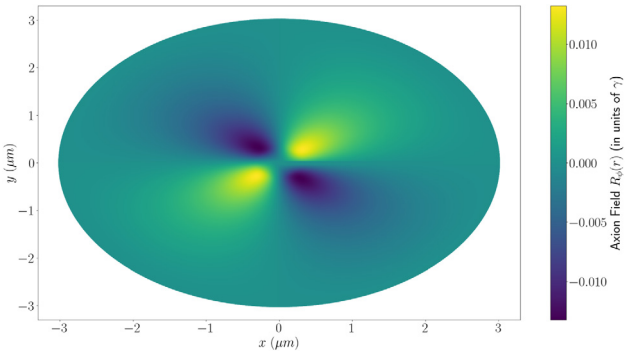

Fig. 9. 2D false color plot for the solution for the hypothetical axion field $u_\phi(r,\theta)$ for the HE_{11} mode ($\beta = 4.16 \times 10^6\ \mathrm{m}^{-1}$) for a fiber with radius $a = 0.3\ \mu\mathrm{m}$ and $n_{\mathrm{core}} = 1.46$ for a laser wavelength $\lambda = 1550\ \mathrm{nm}$ with $\Delta k^2 = -0.89 \times 10^{12}\ \mathrm{m}^{-2}$.

laser and affecting the propagation of a probe laser beam. The existence of axions can then be verified by measuring the change either in the phase or the intensity of the probe laser propagating at a nearby fiber. Using challenging but experimentally realizable parameters, these experiments can put a detection bound on the axion-photon coupling constant $g_{a\gamma\gamma}$ at the level of $10^{-10}\ \mathrm{GeV}^{-1}$ for axions in the mass range $10^{-6}\ \mathrm{eV} < m < 10^{-2}\ \mathrm{eV}$.

In Ref. [57], we discussed the detection bounds on the axion-photon coupling constant $g_{a\gamma\gamma}$, for four different envisioned phases of a future experiment. These detection bounds were calculated using standard transverse modes of an optical fiber utilizing a number of simplifying assumptions for the fiber modes. We have recently quantitatively estimated these detection bounds for the non-transverse EM modes in MNFs, using the axion field similar to what is shown in Fig. 9. A detailed discussion of axion detection bounds using non-transverse EM modes that are discussed in this section will be reported elsewhere [74].

5. NEW TYPE OF OPTICAL TRAP FOR CHIRAL ATOMS WITH MAGNETO-ELECTRIC CROSS COUPLING

A. Chiral Atoms with Magneto-Electric Cross Coupling

Over the last two decades, there has been a growing interest in materials that exhibit chirality through magneto-electric cross coupling. In traditional materials, the electric field of the light produces polarization of the medium while the magnetic field induces magnetization. In contrast, in materials with magneto-electric cross coupling, the electric field can induce magnetization, while the magnetic field can polarize the medium. One application of these materials is to the studies of negative refractive index. Materials that exhibit a negative index of refraction have been a subject of research because of their interesting fundamental properties as well as applications that they demonstrate such as the possibility of constructing lenses whose performance can beat the diffraction limit [59,75–85]. One key challenge in constructing negative index materials is due to the weakness of the magnetic response in optical materials [59]. Chiral materials with magneto-electric cross coupling show considerable promise for overcoming this limitation due to additional contributions of the cross coupling coefficients to the refractive index [86,87]. Using such cross coupling scheme, one can achieve a negative index of refraction without having a negative permeability [59,88,89].

In a material with magneto-electric cross coupling, the polarization, P_p, and the magnetization, M_p, for a probe beam with electric field E_p and the magnetic field with B_p is given by

$$P_p = \epsilon_0 \chi_E E_p + \frac{\xi_{EB}}{c\mu_0} B_p,$$

$$M_p = \frac{\xi_{BE}}{c\mu_0} E_p + \frac{\chi_M}{\mu_0} B_p. \tag{16}$$

Here, the quantities χ_E and χ_M are the electric and the magnetic susceptibilities, and ξ_{EB} and ξ_{BE} are the complex cross coupling (chirality) coefficients [59,88,89].

In this section, we utilize the effect of magneto-electric cross-coupling-induced chirality for achieving a trap potential for atoms that scale with the term $\vec{E} \cdot \vec{B}$. For this purpose, we are going to focus on the specific five level scheme, which was discussed in detail in Ref. [59]. As shown in Fig. 10, we consider an atomic system with a strong magnetic dipole transition with magnetic-moment μ_{gm} near the frequency of the probe laser beam. The system does not have a strong electric-dipole transition near the probe laser's frequency. Instead, the electric dipole response is obtained by using two-photon Raman transitions that are detuned from the dipole-allowed excited state $|e\rangle$ [59]. The two Raman transitions are introduced by using the probe laser and two intense control beams with electric fields E_{c1} and E_{c2}. Because of the difference in the order of involvement of the probe laser in the Raman transitions, this method creates simultaneously an amplifying resonance and an absorbing resonance [59]. One can tune the strength and the position of these two Raman transitions by changing the frequencies and the intensities of the laser beams. The interference of the two resonances produces control of the index of refraction while having a small absorption.

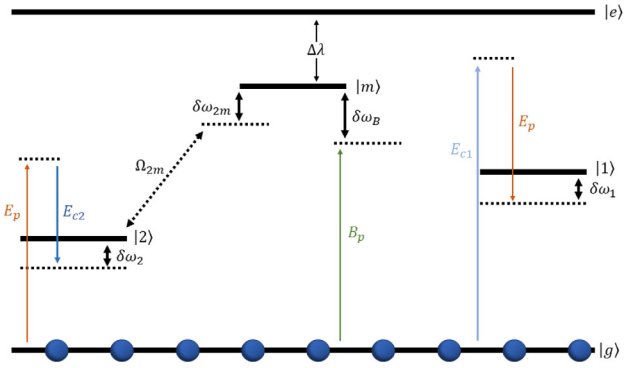

Fig. 10. Energy level diagram of the suggested magneto-electric cross coupling scheme [59]. The electric field E_p and magnetic field B_p are the EM components of the probe laser. $|g\rangle \rightarrow |m\rangle$ is a magnetic dipole transition induced by B_p. Two electric dipole Raman transitions are induced by the two strong control laser beams E_{c1} and E_{c2}. These transitions can be detuned very far away from the excited state $|e\rangle$. Thus the system does not require $|g\rangle \rightarrow |m\rangle$ and $|g\rangle \rightarrow |e\rangle$ transitions to be close to the same frequency. The magneto-electric cross coupling (chirality) is induced by Ω_{2m}.

In this scheme, the coherent coupling of the states $|2\rangle$ and $|m\rangle$ with a separate laser beam with Rabi frequency Ω_{2m} induces magneto-electric cross coupling. The states, $|g\rangle$, $|1\rangle$, $|2\rangle$, and $|m\rangle$ have the same parity, while being the opposite parity to the excited $|e\rangle$ state. We define $\delta\omega_1 = (\omega_1 - \omega_g) - (\omega_{c1} - \omega_p)$ and $\delta\omega_2 = (\omega_2 - \omega_g) - (\omega_p - \omega_{c2})$, which are the two-photon detunings. The detuning of the probe beam for the magnetic transition $|g\rangle \to |m\rangle$ can be defined as $\delta\omega_B = (\omega_m - \omega_g) - \omega_p$. Finally, the detuning of the magneto-electric coupling laser from the transition $|2\rangle \to |m\rangle$ is $\delta\omega_{2m}$. The system forms a closed loop and we therefore have $\delta\omega_B = \delta\omega_2 + \delta\omega_{2m}$. Following these definitions, one can derive the susceptibilities and the chirality coefficients as

$$\chi_E = \frac{N}{\epsilon_0}\left[\frac{|d_{ge}|^2}{\hbar\left(\Delta_p - i\Gamma_e/2\right)} + \frac{|d_{ge}|^2|d_{1e}|^2}{4\hbar^3\Delta_1^2\left(\delta\omega_1 + i\gamma_1\right)}|E_{c1}|^2 + \frac{|d_{ge}|^2|d_{2e}|^2}{4\hbar^3\Delta_2^2\left(\delta\omega_2 - \frac{|\Omega_{2m}|^2}{4(\delta\omega_B - i\gamma_m)} - i\gamma_2\right)}|E_{c2}|^2\right],$$

$$\xi_{EB} = \mu_0 c N \frac{d_{ge}d_{2e}^*\mu_{gm}^*}{4\hbar^2\Delta_2(\delta\omega_B - i\gamma_m)\left(\delta\omega_2 - \frac{|\Omega_{2m}|^2}{4(\delta\omega_B - i\gamma_m)} - i\gamma_2\right)}\Omega_{2m}E_{c2}, \tag{17}$$

with N being the number of atoms per unit volume. Further details of this approach can be found from earlier publications of our group [59].

B. Chiral Trap Potential Scaling with $\vec{E}\cdot\vec{B}$

In this subsection, we introduce a trapping potential for chiral atoms that depends on the $U \propto \vec{E}\cdot\vec{B}$, rather than the conventional dipole trap potential that scales with $U \propto |\vec{E}|^2$. We consider an atom with the above-described magneto-electric cross coupling scheme and, therefore, exhibiting chirality. The trapping potential for such an atom in the presence of the probe laser is

$$\begin{aligned} U_{\text{trap}} &= \frac{1}{N}\langle \vec{E}_p \cdot \vec{P}_p\rangle \\ &= \frac{\epsilon_0 \text{Re}\{\chi_E\}}{2N}|\vec{E}_p|^2 \\ &\quad + \frac{1}{Nc\mu_0}\left(\text{Re}\{\xi_{EB}\}\langle \vec{E}_p \cdot \vec{B}_p\rangle - i\text{Im}\{\xi_{EB}\}\left(E_p B_p^* - E_p^* B_p\right)\right). \end{aligned} \tag{18}$$

Using the results from the previous section and as we will discuss below, we have the freedom to tune the quantities χ_E and ξ_{EB} [59]. Therefore, one can find a condition where $\chi_E \ll \xi_{EB}$ and the trapping potential of Eq. (18) is dominated by the second term. We note that for a trapping potential that is only proportional to $\langle \vec{E}_p \cdot \vec{B}_p\rangle$, because of the sign of the electromagnetic fields, there will be regions where the potential is attractive as well as repulsive. This behavior on its own is interesting and is different from the usual dipole potential $U \propto |\vec{E}|^2$ where depending on the sign of the detuning of the trapping laser from the excited state, the potential is either attractive or repulsive everywhere.

Having discussed the general scheme of the trapping, we proceed with a numerical example in an example atomic system. We choose a vacuum-cladded ($n_{\text{clad}} = 1$) MNF structure with the core radius of $a = 0.2$ μm. We use two probe lasers with wavelengths $\lambda_{p1} = 601$ nm and $\lambda_{p2} = 599$ nm, one red and one blue detuned magnetic-dipole transition at a wavelength of 600 nm, to produce a force that generates attractive and repulsive potential wells and hills. The relevant propagation constants for the modes of these two probe lasers are $\beta_1 = 12.50 \times 10^6\ \text{m}^{-2}$ and $\beta_2 = 14.68 \times 10^6\ \text{m}^{-2}$. We choose parameters that are similar to what could be expected from a real atomic system [90]: we take the excited state decay rate to be $\Gamma_e = 2\pi \times 10$ MHz, and choose two coupling lasers with wavelengths $\lambda_{c1} = 610$ nm and $\lambda_{c2} = 599.9$ nm. We define the detunings as $\delta\omega_B = -\delta\omega_1 = \delta\omega_2$. We introduce a dephasing rate of $\gamma_1 = \gamma_2 = \gamma_m = \gamma_c = 2\pi \times 1$ MHz to the dipole-forbidden transition and take the Rabi frequency of the cross coupling laser to be $\Omega_{2m} = i2\pi \times 2.12$ MHz. We use intensities of $I_{c1} = 0.25\ \text{MW/cm}^2$ and $I_{c2} = 0.7\ \text{MW/cm}^2$ for the two coupling lasers. We also note that for simplicity, the coupling lasers are taken to be uniform while the probe lasers are assumed to be in the evanescent field of the hybrid fiber modes that are analytically shown in Eq. (3). We choose the optical power in the probe laser beams to be 100 mW. Finally, we calculate the electric and magnetic dipole matrix elements using the Wigner-Weisskopf result

$$d_{ij} = \sqrt{\frac{\pi\epsilon_0\Gamma_e\hbar c^3}{\omega_p^3}}, \qquad \mu_{ij} = \sqrt{\frac{\pi\epsilon_0\Gamma_e\hbar c^5}{\omega_p^3 137^2}}. \tag{19}$$

In Fig. 11(a), we plot the real parts of the calculated susceptibilities $\chi_{E1}(\delta\omega)$ (solid blue) and $\chi_{E2}(\delta\omega)$ (solid red) with respect to the detuning (the subscripts "1" and "2" refer to quantities due to the first and the second probe laser, respectively). In this figure, one can notice that as we get close to zero detuning, the susceptibilities behave closely and start diverging in the highly detuned regime. In Fig. 11(b), the real (solid blue) and the imaginary parts (dashed light blue) of the chirality constant ξ_{EB1} along with the real (solid red) and the imaginary parts (dashed green) of the chirality constant ξ_{EB2} are plotted. Since these chirality constants have opposite signs for any detuning, they can be used to balance the trapping potential close to the fiber, thereby preventing the atoms from sticking to the fiber.

To form a trapping potential well, we pick a detuning of $0.36\gamma_m$, which renders the real parts of susceptibilities of the lasers to be $Re\{\chi_{E1}\} = -0.0008$ and $Re\{\chi_{E2}\} = -0.0002$. This specific choice of the detuning suppresses the dipole potential and gives the user the freedom of tuning the chiral trapping potential. Although one can achieve radial trapping by appropriate tuning of the dipole and chiral potentials with

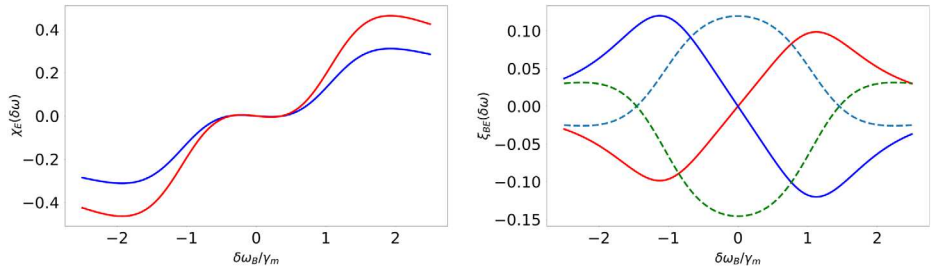

Fig. 11. (a) The real parts of the susceptibilities $\chi_{E1}(\delta\omega)$ (solid blue) and $\chi_{E2}(\delta\omega)$ (solid red) with respect to the detuning $\delta\omega/\gamma_M$ for the probe wavelengths of $\lambda_{p1} = 601$ nm and $\lambda_{p2} = 599$ nm with coupling wavelengths of $\lambda_{c1} = 610$ nm and $\lambda_{c2} = 599.9$ nm. (b) The real and imaginary parts of the chirality constants $\xi_{EB1}(\delta\omega)$ and $\xi_{EB2}(\delta\omega)$ with respect to the detuning $\delta\omega/\gamma_M$ for the probe wavelengths of $\lambda_{p1} = 601$ nm and $\lambda_{p2} = 599$ nm with coupling wavelengths of $\lambda_{c1} = 610$ nm and $\lambda_{c2} = 599.9$ nm. The solid blue and the dashed light blue curves represent the real and the imaginary parts of the chirality constant of the λ_{p1} laser, $\xi_{EB1}(\delta\omega)$. The solid red and the dashed green curves represent the real and imaginary parts of the chirality constant calculated for the laser λ_{p2}, $\xi_{EB2}(\delta\omega)$.

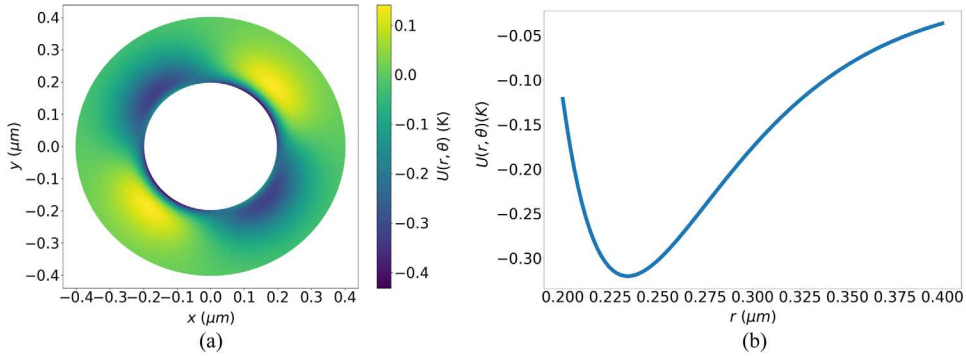

Fig. 12. (a) The false-color plot of the calculation of the chiral trapping potential coming from the two probe beams λ_{p1} and λ_{p2} with the parameters $\Gamma_e = 2\pi \times 10$ MHz, $\lambda_{c1} = 610$ nm, and $\lambda_{c2} = 599.9$ nm, $\gamma_1 = \gamma_2 = \gamma_m = \gamma_c = 2\pi \times 1$ MHz, $\Omega_{2m} = i2\pi \times 2.12$ MHz, $I_{c1} = 0.25$ MW/cm^2, and $I_{c2} = 0.7$ MW/cm^2 with probe lasers' powers being 10 mW. (b) The cross section of the chiral trapping potential at the azimuthal angle $\theta = 2.36\pi$. The trapping potential reaches to 150 mK scales.

only one probe laser beam, the symmetric nature of the dipole force makes azimuthally trapping of particles more difficult. We find that this problem can be overcome by reducing the magnitude of the dipole potential and using two probe lasers, thereby achieving both radial and azimuthal trapping. Furthermore, the trap minimum in the radial direction can be formed sufficiently far away from the fiber so that the atoms do not stick to the fiber surface.

With the above chosen parameters that are close to the parameters used in our previous paper [59], we use Eq. (18) and calculate the total trapping potential. In Fig. 12(a), we show a 2D false-color plot of the total chiral trapping potential coming from the two probe lasers with λ_{p1} and λ_{p2}. The plot demonstrates attractive and repulsive regions along the azimuthal direction. In Fig. 12(b), a cross section of the total potential taken at the azimuthal angle $\theta = 2.36\pi$ with respect to the radial distance from the fiber core is plotted. Here, we observe that an attractive potential well with a maximum trap depth of 150 mK can be achieved with 100 mW probe lasers.

We note that because the modes that we discuss are propagating EM modes along the fiber, the $\vec{E} \cdot \vec{B}$ trapping potential is independent of the propagation axis, z. As a result, there is no trapping along the longitudinal z direction of the fiber. This issue can be resolved by using a number of different approaches. For example, a second wave propagating along the $-z$ axis can be used (a counter-propagating mode), which would then form a standing wave along the z axis and produce a $\cos^2(kz)$ type potential. Another approach would be to taper the fiber along the longitudinal z direction so that the modes vary as a function of the propagation direction.

In this section, we have demonstrated a novel type of atom trapping that utilizes the chiral force occurring from the magneto-electric cross coupling of atoms. With choosing special detunings, one can neglect the dipole force and achieve attractive and repulsive potentials for trapping atoms with fibers. This scheme can be achieved with atoms that demonstrate magneto-electric cross coupling such as erbium, terbium, or dysprosium [59]. In another previous paper [91], we discuss achieving a negative index of refraction with the magneto-electric cross coupling effect for terbium atoms. Interested readers can also find further information about this topic and possible experimental applications in a comprehensive review by our group [90] as well. In addition, cooling these atoms down is another challenge for the possible experimental realization of this trapping scheme. Thankfully, magneto-optical traps for erbium [92–94] and dysprosium [95–97] such as other lanthanoid atoms [98–100], as well as a dual species MOT of Er and Dy [101] have been previously reported. With such MOT structures along with a magneto-electric cross coupling scheme and a tapered

fiber structure, it may be possible to experimentally observe such traps in the near future.

6. CONCLUSIONS

In conclusion, we have presented an analytical and numerical study of electromagnetic modes in micro- and nano-fibers (MNFs) where the electric and magnetic fields of the propagating modes are not orthogonal to each other. We have also discussed applications of these modes in searching for hypothetical particles such as axions and in forming new types of optical traps for chiral atoms with magneto-electric cross coupling.

One immediate future direction is to experimentally demonstrate optical traps where the confining potential is proportional to $\vec{E} \cdot \vec{B}$. To demonstrate such traps, one approach would be to place the fiber structures that we have discussed above inside laser cooled atomic ensembles where magneto-electric cross coupling can be induced, for example, lanthanides such as terbium or dysprosium. Another future direction is to integrate the above discussed fiber structures to proposed fiber and laser based axion searches and evaluate the bounds on axion-photon coupling that such experiments would place under realistic experimental conditions [57].

Funding. National Science Foundation (2016136); University of Wisconsin-Madison (Research Forward I Award).

Acknowledgment. We thank Robby Rozite, Shay Inbar, and David Gold for many helpful discussions.

Disclosures. The authors declare no conflicts of interest.

Data availability. The numerical data generated through COMSOL underlying the results presented in this paper are not publicly available at this time but may be obtained from the authors upon reasonable request.

REFERENCES

1. L. Zhang, Y. Tang, and L. Tong, "Micro-/nanofiber optics: merging photonics and material science on nanoscale for advanced sensing technology," iScience **23**, 100810 (2020).
2. L. Tong and M. Sumetsky, "Subwavelength and nanometer diameter optical fibers," in *Advanced Topics in Science and Technology in China* (Springer, 2010).
3. M. Sumetsky, "How thin can a microfiber be and still guide light?" Opt. Lett. **31**, 870–872 (2006).
4. B. Lee, "Review of the present status of optical fiber sensors," Opt. Fiber Technol. **9**, 57–79 (2003).
5. F. Le Kien, V. I. Balykin, and K. Hakuta, "Atom trap and waveguide using a two-color evanescent light field around a subwavelength-diameter optical fiber," Phys. Rev. A **70**, 063403 (2004).
6. M. J. Renn, D. Montgomery, O. Vdovin, *et al.*, "Laser-guided atoms in hollow-core optical fibers," Phys. Rev. Lett. **75**, 3253–3256 (1995).
7. H. Ito, K. Sakaki, M. Ohtsu, *et al.*, "Evanescent-light guiding of atoms through hollow optical fiber for optically controlled atomic deposition," Appl. Phys. Lett. **70**, 2496–2498 (1997).
8. M. Ol'Shanii, Y. Ovchinnikov, and V. Letokhov, "Laser guiding of atoms in a hollow optical fiber," Opt. Commun. **98**, 77–79 (1993).
9. J. P. Dowling and J. Gea-Banacloche, "Evanescent light-wave atom mirrors, resonators, waveguides, and traps," in *Advances in Atomic, Molecular, and Optical Physics* (Elsevier, 1996), pp. 1–94.
10. S. Marksteiner, C. M. Savage, P. Zoller, *et al.*, "Coherent atomic waveguides from hollow optical fibers: quantized atomic motion," Phys. Rev. A **50**, 2680–2690 (1994).
11. M. Daly, V. G. Truong, C. F. Phelan, *et al.*, "Nanostructured optical nanofibres for atom trapping," New J. Phys. **16**, 053052 (2014).
12. Y. B. Ovchinnikov, S. V. Shulga, and V. I. Balykin, "An atomic trap based on evanescent light waves," J. Phys. B **24**, 3173 (1991).
13. R. Kumar, V. Gokhroo, K. Deasy, *et al.*, "Interaction of laser-cooled 87Rb atoms with higher order modes of an optical nanofibre," New J. Phys. **17**, 013026 (2015).
14. K. Hakuta and K. P. Nayak, "Manipulating single atoms and photons using optical nanofibers," Adv. Nat. Sci. **3**, 015005 (2012).
15. A. Goban, K. S. Choi, D. J. Alton, *et al.*, "Demonstration of a state-insensitive, compensated nanofiber trap," Phys. Rev. Lett. **109**, 033603 (2012).
16. E. Vetsch, D. Reitz, G. Sagué, *et al.*, "Optical interface created by laser-cooled atoms trapped in the evanescent field surrounding an optical nanofiber," Phys. Rev. Lett. **104**, 203603 (2010).
17. V. I. Balykin, V. S. Letokhov, Y. B. Ovchinnikov, *et al.*, "Quantum-state-selective mirror reflection of atoms by laser light," Phys. Rev. Lett. **61**, 902 (1988).
18. S. Tojo and M. Hasuo, "Oscillator-strength enhancement of electric-dipole-forbidden transitions in evanescent light at total reflection," Phys. Rev. A **71**, 012508 (2005).
19. S. Tojo, T. Fujimoto, and M. Hasuo, "Precision measurement of the oscillator strength of the cesium $6^2s_{1/2} \rightarrow 5^2d_{5/2}$ electric quadrupole transition in propagating and evanescent wave fields," Phys. Rev. A **71**, 012507 (2005).
20. S. Tojo, M. Hasuo, and T. Fujimoto, "Absorption enhancement of an electric quadrupole transition of cesium atoms in an evanescent field," Phys. Rev. Lett. **92**, 053001 (2004).
21. F. Le Kien, T. Ray, T. Nieddu, *et al.*, "Enhancement of the quadrupole interaction of an atom with the guided light of an ultrathin optical fiber," Phys. Rev. A **97**, 013821 (2018).
22. T. Ray, R. K. Gupta, V. Gokhroo, *et al.*, "Observation of the 87Rb 5s1/2 to 4d3/2 electric quadrupole transition at 516.6 nm mediated via an optical nanofibre," New J. Phys. **22**, 062001 (2020).
23. D. C. Gold, A. S. Bhadkamkar, S. Carpenter, *et al.*, "High-power near-cw Raman lasing in mm-sized glass disks," Opt. Lett. **47**, 4171–4174 (2022).
24. J. T. Karpel, D. C. Gold, and D. D. Yavuz, "Prospects for continuous-wave molecular modulation in Raman-active microresonators," Opt. Express **27**, 34154–34168 (2019).
25. A. W. Snyder and J. D. Love, *Optical Waveguide Theory*, 1983rd ed. (Chapman and Hall, 1983).
26. H. Zaghloul and H. A. Buckmaster, "Transverse electromagnetic standing waves with $e \parallel b$," Am. J. Phys. **56**, 801–806 (1988).
27. K. Uehara, T. Kawai, and K. Shimoda, "Non-transverse electromagnetic waves with parallel electric and magnetic fields," J. Phys. Soc. Jpn. **58**, 3570–3575 (1989).
28. K. Shimoda, T. Kawai, and K. Uehara, "Electromagnetic plane waves with parallel electric and magnetic fields $e \parallel h$ in free space," Am. J. Phys. **58**, 394–396 (1990).
29. T. Nishiyama, "General plane or spherical electromagnetic waves with electric and magnetic fields parallel to each other," Wave Motion **54**, 58–65 (2015).
30. R. Mochizuki, N. Shinohara, and A. Sanada, "Time-harmonic electromagnetic fields with $e \parallel h$ represented by superposing two counter-propogating Beltrami fields," Prog. Electromagn. Res. M **104**, 171–183 (2021).
31. C. Chu and T. Ohkawa, "Transverse electromagnetic waves with $\vec{e} \parallel \vec{b}$," Phys. Rev. Lett. **48**, 837–838 (1982).
32. K. K. Lee, "Comments on "transverse electromagnetic waves with $\vec{e} \parallel \vec{b}$," Phys. Rev. Lett. **50**, 138 (1983).
33. C. Chu, "Chu responds," Phys. Rev. Lett. **50**, 139 (1983).
34. H. Zaghloul, K. Volk, and H. A. Buckmaster, "Comment on "transverse electromagnetic waves with $e \parallel b$"," Phys. Rev. Lett. **58**, 423 (1987).
35. C. Chu and T. Ohkawa, "Chu and Ohkawa respond," Phys. Rev. Lett. **58**, 424 (1987).
36. F. C. Michel, "Transverse electromagnetic waves with nonzero $\vec{e} \cdot \vec{b}$," Phys. Rev. Lett. **52**, 1351 (1984).

37. V. Evtuhov and A. E. Siegman, "A "twisted-mode" technique for obtaining axially uniform energy density in a laser cavity," Appl. Opt. **4**, 142–143 (1965).
38. D. Draegert, "Efficient single-longitudinal-mode nd:YAG laser," IEEE J. Quantum Electron. **8**, 235–239 (1972).
39. D. D. Jong and D. Andreou, "An nd:YAG laser whose active medium experiences no hole burning effects," Opt. Commun. **22**, 138–142 (1977).
40. P. Polynkin, A. Polynkin, M. Mansuripur, *et al.*, "Single-frequency laser oscillator with watts-level output power at 15 μm by use of a twisted-mode technique," Opt. Lett. **30**, 2745–2747 (2005).
41. Y. Zhang, C. Gao, M. Gao, *et al.*, "A diode pumped tunable single-frequency Tm:YAG laser using twisted-mode technique," Laser Phys. Lett. **7**, 17–20 (2010).
42. E. L. Raab, M. Prentiss, A. Cable, *et al.*, "Trapping of neutral sodium atoms with radiation pressure," Phys. Rev. Lett. **59**, 2631–2634 (1987).
43. L. Woltjer, "A theorem on force-free magnetic fields," Proc. Natl. Acad. Sci. USA **44**, 489–491 (1958).
44. F. Wilczek, "Two applications of axion electrodynamics," Phys. Rev. Lett. **58**, 1799–1802 (1987).
45. R. D. Peccei and H. R. Quinn, "Conservation in the presence of pseudoparticles," Phys. Rev. Lett. **38**, 1440–1443 (1977).
46. R. D. Peccei and H. R. Quinn, "Constraints imposed by CP conservation in the presence of pseudoparticles," Phys. Rev. D **16**, 1791–1797 (1977).
47. P. W. Graham, I. G. Irastorza, S. K. Lamoreaux, *et al.*, "Experimental searches for the axion and axion-like particles," Annu. Rev. Nucl. Part. Sci. **65**, 485–514 (2015).
48. M. S. Safronova, D. Budker, D. DeMille, *et al.*, "Search for new physics with atoms and molecules," Rev. Mod. Phys. **90**, 025008 (2018).
49. D. Budker, P. W. Graham, M. Ledbetter, *et al.*, "Proposal for a cosmic axion spin precession experiment (CASPER)," Phys. Rev. X **4**, 021030 (2014).
50. I. G. Irastorza and J. Redondo, "New experimental approaches in the search for axion-like particles," Prog. Part. Nucl. Phys. **102**, 89–159 (2018).
51. J. Preskill, M. B. Wise, and F. Wilczek, "Cosmology of the invisible axion," Phys. Lett. B **120**, 127–132 (1983).
52. L. Abbott and P. Sikivie, "A cosmological bound on the invisible axion," Phys. Lett. B **120**, 133–136 (1983).
53. M. Dine and W. Fischler, "The not-so-harmless axion," Phys. Lett. B **120**, 137–141 (1983).
54. M. Gasperini, "Axion production by electromagnetic fields," Phys. Rev. Lett. **59**, 396–398 (1987).
55. L. Visinelli, "Dual axion electrodynamics," arXiv (2011).
56. M. C. Huang and P. Sikivie, "Structure of axionic domain walls," Phys. Rev. D **32**, 1560–1568 (1985).
57. D. D. Yavuz and S. Inbar, "Generation and detection of axions using guided structures," Phys. Rev. D **105**, 074012 (2022).
58. COMSOL, "Wave optics module user's guide," COMSOL, 6th ed., 2022, available at https://doc.comsol.com/6.1/doc/com.comsol.help.woptics/WaveOpticsModuleUsersGuide.pdf.
59. D. E. Sikes and D. D. Yavuz, "Negative refraction with low absorption using Raman transitions with magnetoelectric coupling," Phys. Rev. A **82**, 011806 (2010).
60. B. E. A. Saleh and M. C. Teich, *Fundamentals of Photonics* (Wiley, 1991).
61. F. L. Pedrotti, L. M. Pedrotti, and L. S. Pedrotti, *Introduction to Optics*, 3rd ed. (Cambridge University, 2017).
62. K. Okamoto, *Preface to the Second Edition* (Elsevier, 2006).
63. S. John, "Strong localization of photons in certain disordered dielectric superlattices," Phys. Rev. Lett. **58**, 2486–2489 (1987).
64. E. Yablonovitch, "Inhibited spontaneous emission in solid-state physics and electronics," Phys. Rev. Lett. **58**, 2059–2062 (1987).
65. P. Sikivie, "Experimental tests of the "invisible" axion," Phys. Rev. Lett. **51**, 1415–1417 (1983).
66. L. Krauss, J. Moody, F. Wilczek, *et al.*, "Calculations for cosmic axion detection," Phys. Rev. Lett. **55**, 1797–1800 (1985).
67. L. Maiani, R. Petronzio, and E. Zavattini, "Effects of nearly massless, spin-zero particles on light propagation in a magnetic field," Phys. Lett. B **175**, 359–363 (1986).
68. S. DePanfilis, A. C. Melissinos, B. E. Moskowitz, *et al.*, "Limits on the abundance and coupling of cosmic axions at $4.5 < m_a < 5.0$ μev," Phys. Rev. Lett. **59**, 839–842 (1987).
69. W. U. Wuensch, S. De Panfilis-Wuensch, Y. K. Semertzidis, *et al.*, "Results of a laboratory search for cosmic axions and other weakly coupled light particles," Phys. Rev. D **40**, 3153–3167 (1989).
70. K. Zioutas, C. Aalseth, D. Abriola, *et al.*, "A decommissioned LHC model magnet as an axion telescope," Nucl. Instrum. Methods Phys. Res. A **425**, 480–487 (1999).
71. E. Armengaud, F. T. Avignone, M. Betz, *et al.*, "Conceptual design of the international axion observatory (IAXO)," J. Instrum. **9**, T05002 (2014).
72. K. Ehret, M. Frede, S. Ghazaryan, *et al.*, "New alps results on hidden-sector lightweights," Phys. Lett. B **689**, 149–155 (2010).
73. H. Tam and Q. Yang, "Production and detection of axion-like particles by interferometry," Phys. Lett. B **716**, 435–440 (2012).
74. R. Rozite, U. Saglam, and D. D. Yavuz, Department of Physics, University of Wisconsin—Madison, 1150 University Avenue, Madison, Wisconsin 53706, USA, are preparing a manuscript to be called "Generation and detection of axions using non-transverse modes."
75. V. G. Veselago, "The electrodynamics of substances with simultaneously negative values of and μ," Sov. Phys. Usp. **10**, 509 (1968).
76. J. B. Pendry, "Negative refraction makes a perfect lens," Phys. Rev. Lett. **85**, 3966–3969 (2000).
77. D. R. Smith and N. Kroll, "Negative refractive index in left-handed materials," Phys. Rev. Lett. **85**, 2933–2936 (2000).
78. S. Foteinopoulou, E. N. Economou, and C. M. Soukoulis, "Refraction in media with a negative refractive index," Phys. Rev. Lett. **90**, 107402 (2003).
79. R. A. Shelby, D. R. Smith, and S. Schultz, "Experimental verification of a negative index of refraction," Science **292**, 77–79 (2001).
80. A. A. Houck, J. B. Brock, and I. L. Chuang, "Experimental observations of a left-handed material that obeys Snell's law," Phys. Rev. Lett. **90**, 137401 (2003).
81. E. Cubukcu, K. Aydin, E. Ozbay, *et al.*, "Negative refraction by photonic crystals," Nature **423**, 604–605 (2003).
82. N. Fang, H. Lee, C. Sun, *et al.*, "Sub-diffraction-limited optical imaging with a silver superlens," Science **308**, 534–537 (2005).
83. V. M. Shalaev, W. Cai, U. K. Chettiar, *et al.*, "Negative index of refraction in optical metamaterials," Opt. Lett. **30**, 3356 (2005).
84. S. Zhang, W. Fan, N. C. Panoiu, *et al.*, "Experimental demonstration of near-infrared negative-index metamaterials," Phys. Rev. Lett. **95**, 137404 (2005).
85. G. Dolling, M. Wegener, C. M. Soukoulis, *et al.*, "Negative-index metamaterial at 780 nm wavelength," Opt. Lett. **32**, 53–55 (2006).
86. J. B. Pendry, "A chiral route to negative refraction," Science **306**, 1353–1355 (2004).
87. C. Monzon and D. W. Forester, "Negative refraction and focusing of circularly polarized waves in optically active media," Phys. Rev. Lett. **95**, 123904 (2005).
88. J. Kästel, M. Fleischhauer, S. F. Yelin, *et al.*, "Tunable negative refraction without absorption via electromagnetically induced chirality," Phys. Rev. Lett. **99**, 073602 (2007).
89. J. Kästel, M. Fleischhauer, S. F. Yelin, *et al.*, "Low-loss negative refraction by laser-induced magnetoelectric cross coupling," Phys. Rev. A **79**, 063818 (2009).
90. Z. N. Buckholtz and D. D. Yavuz, "Negative refraction in terbium at ultraviolet frequencies," Opt. Lett. **45**, 5049–5052 (2020).
91. D. D. Yavuz and Z. N. Buckholtz, "Negative index materials using atomic transitions: progress and challenges," in *Advances in Atomic, Molecular, and Optical Physics* (Academic, 2018), Chap. 8, pp. 429–464.
92. A. J. Berglund, S. A. Lee, and J. J. McClelland, "Sub-Doppler laser cooling and magnetic trapping of erbium," Phys. Rev. A **76**, 053418 (2007).
93. A. Frisch, K. Aikawa, M. Mark, *et al.*, "Narrow-line magneto-optical trap for erbium," Phys. Rev. A **85**, 051401 (2012).
94. J. Ulitzsch, D. Babik, R. Roell, *et al.*, "Bose-Einstein condensation of erbium atoms in a quasielectrostatic optical dipole trap," Phys. Rev. A **95**, 043614 (2017).

95. M. Lu, S. H. Youn, and B. L. Lev, "Trapping ultracold dysprosium: a highly magnetic gas for dipolar physics," Phys. Rev. Lett. **104**, 063001 (2010).
96. T. Maier, H. Kadau, M. Schmitt, *et al.*, "Narrow-line magneto-optical trap for dysprosium atoms," Opt. Lett. **39**, 3138–3141 (2014).
97. D. Dreon, L. A. Sidorenkov, C. Bouazza, *et al.*, "Optical cooling and trapping of highly magnetic atoms: the benefits of a spontaneous spin polarization," J. Phys. B **50**, 065005 (2017).
98. T. Kuwamoto, K. Honda, Y. Takahashi, *et al.*, "Magneto-optical trapping of Yb atoms using an intercombination transition," Phys. Rev. A **60**, R745–R748 (1999).
99. D. Sukachev, A. Sokolov, K. Chebakov, *et al.*, "Magneto-optical trap for thulium atoms," Phys. Rev. A **82**, 011405 (2010).
100. J. Miao, J. Hostetter, G. Stratis, *et al.*, "Magneto-optical trapping of holmium atoms," Phys. Rev. A **89**, 041401 (2014).
101. P. Ilzhöfer, G. Durastante, A. Patscheider, *et al.*, "Two-species five-beam magneto-optical trap for erbium and dysprosium," Phys. Rev. A **97**, 023633 (2018).